Science

AAAS

Supplementary Materials for

A dynamic saline groundwater system mapped beneath an Antarctic ice stream

Chloe D. Gustafson *et al*.

Corresponding author: Chloe D. Gustafson, cgustafson@ucsd.edu

The PDF file includes:

Materials and Methods
Figs. S1 to S7
Tables S1 to S3
References

Materials and Methods

MT data collection

We collected 44 MT soundings over the course of a six-week field campaign in the 2018/2019 austral summer. Our four-person field team deployed all instruments and operated the field camp. We made MT electric and magnetic field measurements using two different wideband systems primarily designed by Phoenix Geophysics Ltd. and Zonge International Inc. Like previous polar MT surveys, we made electric field measurements using high impedance buffer pre-amplifiers connected to titanium plate electrodes, a setup specifically designed for making accurate measurements given the high contact resistance of snow, firn, and ice (*18*, *47–50*). We measured magnetic fields using induction coil magnetometers. Our MT site layout is analogous to the standard '+' bipole array with the sensors aligned parallel and perpendicular to geomagnetic north. We buried our electrodes and magnetometers within the top 0.2 to 0.4 m of firn and sampled data at 1024 Hz (Zonge instruments) or 20,000 Hz (Phoenix instruments). Each station recorded for at least 20 hours in order to obtain periods sensitive to the hydrologic and geologic variations of the upper ~5 km of the subsurface. We deployed and recovered 16 MT stations at our WGZ field site over the course of 13 days (11-Nov-2018 to 06-Dec-2018 UTC) and 27 MT stations at our SLW field site over the course of 11 days (11-Dec-2018 to 23-Dec-2018), when more favorable weather (i.e., lower wind speeds) contributed to more efficient field operations (Fig. 1B, 1C).

MT responses

We obtained MT impedance (Z, a 2 x 2 complex-valued tensor) responses for each station using a robust multivariate processing method (*51*). Prior to the statistical impedance estimation, we

applied a wind-based pre-filtering scheme to remove occasional noisy time-frequency sections of the spectral coefficients that were impacted by high-amplitude wind noise on the electric fields (*18*) (Table S1). This filtering scheme yielded low-noise impedance response functions for periods 0.02–400 s.

We used the rotationally invariant impedance tensor skew (*52*) to determine which periods are most impacted by 3D induction effects. Skews less than 0.2 at periods under 10 s at SLW and under 65 s at WGZ indicate these data are compatible with 2D modeling, whereas higher skews at longer periods indicate sensitivity to deeper geologic 3D variations. Since the focus of this study is on the subglacial hydrology in the upper few kilometers below the ice bed, here we analyzed only the shorter period, 2D compatible data subset.

Two-dimensional MT data can be characterized by two independent modes: transverse magnetic (TM) and transverse electric (TE). In TM mode, electric currents flow in the plane perpendicular to 2D strike, whereas in TE mode, electric currents flow parallel to the 2D strike. For the coordinate reference frame used in our modeling, where the y axis was in-line with each profile of MT stations and the x axis was perpendicular to the profile, we assigned the TM and TE modes to the off-diagonal elements of the impedance tensor Z_{yx} and Z_{xy}, respectively. We transformed the off-diagonal impedance responses to apparent resistivity and phase (*17*) for analysis and modeling.

The MT responses exhibit apparent resistivity steeply dropping at short periods, reaching a minimum around 1–10 s, depending on the station and then rising at longer periods; this behavior

is consistent with a highly resistive ice layer overlying a shallow low-resistivity layer and a deeper high-resistivity basement (Fig S1). More subtle variations of the minimum apparent resistivity and the period range at which it occurs indicate lateral changes in both the thickness and resistivity of the low-resistivity layer. For example, MT stations above the SLW water column and on the floating ice side of the WGZ profile have lower apparent resistivity minimums compared to off-lake/grounded stations (Fig. S1). The MT responses generally have a negligible split between the off-diagonal impedance modes at short periods, implying 1D conductivity layering, whereas the modes begin to split at longer periods, suggesting 2D or 3D induction (Fig. S1).

2D regularized MT inversion

We inverted the data using MARE2DEM (*53*), a goal-oriented adaptive finite element electromagnetic modeling code that uses a non-linear regularized inversion scheme to solve for a smooth model that fits the data. Prior to inversion, we applied a 10% error floor to data at all periods and removed clear outliers. We inverted the data along each of the profiles within the grid of MT stations for the lettered rows and numbered columns of our survey grids (see Figs S5 and S6 profile letter and number labels). Individual station names are alphanumeric and correspond to the letter and number of the two lines that intersect the station location (e.g., station K15 is where the K and 15 profiles intersect). For each inverted data profile, we assigned the 2D model strike (x axis) to be perpendicular to the profile and the data were rotated accordingly (see previous section "MT responses").

For all SLW profiles and the WGZ 16 profile, we inverted both TE and TM mode data, whereas for the L profile at WGZ we inverted only the TM data. We chose to perform a TM-only inversion because TM data are less sensitive to off-profile 3D effects (*17*), which we expect to be present given the complex geometry of the WGZ grounding line embayment (Fig. 1C). In particular, the depressed apparent resistivity at periods > 3s in data assigned to be the TE mode for the WGZ L profile (Fig. S1B) is suggestive of 3D effects from off-profile lateral resistivity boundaries, as there is a strong similarity of this data feature to grounding zone edge-effects seen in TM responses in 2D model studies of the grounding zone (*15*). This correspondence suggests that the long-period "TE" data are sensing the off-profile proximity of the embayment boundary and thus are incompatible with 2D modeling assumptions. Further, we attempted inverting both modes for the WGZ L profile, but these data were incompatible with a 10 m ocean cavity, which is a known feature of this region (*21*, *24*); inverting only the TM data produces a model compatible with the ocean cavity. Although SLW is also a 3D water feature, seawater at WGZ is 46 times less resistive than the SLW lake water (*25*) and thus the ocean cavity in the WGZ embayment creates a much stronger 3D effect in the MT data. Furthermore, the resistivity of the water contained in SLW (14 ohm-m) (*25*) falls within the range of inverted sediment bulk resistivity below SLW (9–25 ohm-m, Fig. 2C) and thus does not present a strong 3D contrast.

The starting model for each inversion consisted of an ice layer over a subglacial region, with ice elevation and thickness extracted from BedMachine Antarctica (*54*), which overall agrees with ground-based radar-derived elevations and thicknesses in our study areas (*4*, *21*). We opted to use BedMachine Antarctica because we were able to extract topography extending several kilometers outside of the model grid of MT stations, which is needed for building the model

grid. We discretized the ice and subglacial regions into a grid of unconstrained free parameters about 200 x 10 m in size and used a starting value of 1 ohm-m for all parameters. Across the ice-bed interface, we relaxed the inversion's spatial roughness penalty constraint so that the resistivity can have a sharp contrast vertically, as the glacial sediments are orders of magnitude less resistive than the overlying ice. Although such a sharp contrast is geologically likely, it is not sharply resolvable by the MT data alone (*17*). For the WGZ L profile, we additionally limited the ocean cavity resistivity values to fall between 0.29–0.31 ohm-m, consistent with in situ observations of ocean salinity (*24*). We also applied a horizontal to vertical smoothing ratio weight of 20 to the roughness penalty to encourage the inversion to find a vertically stratified model everywhere except where lateral variations are required to fit the data. Our model grids contain 30,545 to 36,879 free parameters and 212 to 496 data were inverted, depending on the profile (Tables S2, S3).

All inversions fit the MT data to a root-mean-square (RMS) misfit of 1.0 within 5 to 14 iterations. Figures 2A and 2B show the resulting inversion models for the profiles interpreted in the main text; the corresponding model responses and inverted data are shown in Fig. S1. Despite starting from a 1 ohm-m halfspace, all inversion quickly assigned the ice resistivity to expected values around 500–10,000 ohm-m (*55*), which is required to fit the steep decay of the short period apparent resistivity data (Fig. S1). Below the high-resistivity ice layer, the models contain a low-resistivity zone overlying a deeper resistive zone. Figures S5 and S6 show fence plots of the subglacial sections for all inversion profiles at the SLW and WGZ MT survey locations. From these fence plots we can see there is good agreement across the 2D resistivity models. The depth of the dark conductive band is consistent between models at all intersections,

and the transition to resistive bedrock is also in good agreement at model intersections. This consistency between independent, perpendicular inversions indicates that our 2D modeling is sufficient for imaging the upper ~5 km of the sub-ice environment and that more computationally expensive 3D inversions are not required.

Bayesian model uncertainty analysis and minimum sediment thickness estimation

We used a 1D transdimensional Bayesian inversion method (56) to examine the non-linear uncertainty in inverted resistivity. These results highlight which features of the 2D regularized inversions are statistically robust and help resolve the sediment layer thickness. We inverted the Z_{yx} mode response for each SLW K profile and each WGZ L profile station individually using wide, uniform prior distributions, with ice resistivity bound between 10^3 to 10^8 ohm-m and the subglacial resistivity bound between 10^{-2} to 10^4 ohm-m. As expected, the Bayesian results show the MT data best resolve the low-resistivity layer beneath the ice, as indicated by the tightly constrained 90% credible interval defined by the red lines showing the 5th and 95th percentiles of the resistivity probability distribution (Fig. S4). We used the depth where the steep positive gradient in the 95th percentile (right-most red line in Fig. S4) crosses 100 ohm-m to define the minimum sediment thickness required beneath each station, as above this depth, only low-resistivity values (which we interpret to be water saturated sediments) are compatible with the data.

Results for the SLW K profile stations K08 to K15 exhibit two distinct regions of high probability (lighter colors), one near 1 km depth centered on 10 ohm-m and the other near 1.7 km depth centered on 1 ohm-m. Conversely, stations K18 and K21 show one low resistivity,

high probability region at 1.1 and 1 km depth, respectively, with resistivity values near 5 ohm-m. The results for the WGZ L profile data (Fig. S2) show that the data require a low-resistivity layer below the ice base, but generally do not require a further decrease in resistivity with depth, similar to SLW. The region of high probability ranges from 3 to 10 ohm-m for WGZ sites. For both SLW and WGZ, the 2D inversion profiles (yellow lines in Fig S4) generally fall within the 90% credible interval for most stations, with the Bayesian analyses providing a confidence interval proxy for the 2D results. The low-resistivity ocean cavity, which we imposed as fixed structure in the 2D gradient-based inversions, did not appear within the 90% credible interval in the Bayesian inversions, indicating that the data are relatively insensitive to the small integrated conductance represented by the thin ocean cavity.

Converting sediments bulk resistivity to groundwater salinity

Low resistivity features in electromagnetic modeling are geologically non-unique and prior information is necessary to determine the cause of low resistivity. Considering the direct constraints on the shallow porewater chemistry, which suggest an increase in groundwater salinity with depth (*25*), the measured geothermal heat flux from WIS (*30*), and the porosity of marine sediments from the front of Ross Ice Shelf (*29*) (which are likely of similar origin to the sediments of our survey region), we interpret the low resistivity layer in our models to be water saturated sediments that have increasing porewater salinity with depth. Low resistivity in sediments can also be explained by the presence of conductive clays; however, clay resistivity typically exceeds 5 ohm-m (*57*, *58*), and the minimum resistivity value at both SLW and WGZ is ~1 ohm-m. This suggests our observed low resistivities arise from pore water with high ionic

strength. Even if clays are present within the deep sediments, their effect on resistivity is negligible when saline pore water is present (*59*).

We applied Archie's empirical law (*60*) to convert the observed resistivity into pore fluid resistivity estimates:

$$\rho_f = \rho\phi^m,$$

where ρ_f is the pore fluid resistivity, ρ is the bulk resistivity imaged by our MT inversions, ϕ is the sediment porosity, and *m* is the cementation factor. The derived ρ_f can then be converted to salinity via the Practical Salinity Scale, a method for computing a unitless water salinity given its temperature and electrical conductivity (*61*). We applied Archie's law using *m* = 1.5–2.5 (Fig. 2C, 2D), values which fall within the typical range for sedimentary rocks (*62*). We also assumed a 50 ºC/km temperature gradient (*30*). For ϕ, we assign the top of the basal sediments a porosity of 0.43, consistent with porosity measurements directly beneath SLW (*39*) and other Siple Coast ice streams (*5*), and assume an exponential porosity decrease with depth consistent with sediment compaction (*63*):

$$\phi(z) = a + (\phi_0 - a)e^{-zb},$$

where $a = 0.05$ is the minimum porosity, z is depth relative to the ice bed, $\phi_0 = 0.43$ is the initial porosity at the surface, *z* is depth relative to the ice bed, and $b = 4.7347 \times 10^{-4}$ is the porosity decay exponent. Because there are currently no deep subglacial sediment cores available, we choose a porosity decay term consistent with porosity observations from deeply drilled Ross Sea sediments (*29*). The estimated salinity profiles are shown in Fig. 2C, 2D. If we were to choose a larger porosity decay exponent, the estimated salinity at depth would increase, whereas a smaller

porosity decay exponent would decrease the estimated salinity at depth, but overall the trend of increasing groundwater salinity would remain.

Rationale for rapid salinization of sediments

We argue that the elevated porewater salinity at the bottom of the sediments is partly due to rapid salinization of the entire sediment column from a marine incursion during the mid-Holocene (*33, 34*). Numerical modeling suggests that marine inundations can cause salinization of thick high permeability sediments over the course of decades via free convection (*35*). We computed time to salinization for 0.1, 0.25, 0.5 and 1.0 km thick sediment columns given a range of permeabilities and a seawater fraction of 0.5 using equations 14 and 15 in ref. (*35*). These results show that sediments can be salinized in under 1000 years for permeabilities greater than 10^{-12} m^2 or in less than 100,000 years for permeabilities greater than 10^{-14} m^2 (Fig. S7). Active source seismic imaging reveals gently dipping layers of strata, suggesting that the vast majority of the sediment thickness is composed of sediments deposited in a marine setting, thus relatively low permeabilities associated with subglacial till are likely restricted to the upper few meters of the sediment column (*64*). This deep salty water may additionally be composed of much older seawater that was emplaced over a long period of time when open ocean conditions were persistent in our survey regions (*65*): the emplacement of salty groundwater could have coincided with the deposition of marine sediments, as pore waters would have inherited the salinity of the bottom water (seawater).

Other possible mechanisms for enhanced groundwater salinity at depth

Although a mid-Holocene marine incursion is our preferred mechanism for the most recent salty groundwater emplacement, other possible sources include subaerial evaporation of seawater, marine aerosol mixing, dissolution of buried evaporitic deposits, and cryoconcentration (*66*). Given that the marine sediments in our survey regions are below sea level, subaerial evaporation and marine aerosols are unlikely to have increased the groundwater salinity. Evaporite deposits are often associated with rifted margins, suggesting the possibility that such deposits may have been laid down in transient closed basins formed by the active West Antarctic rift system some time from onset of rifting in the late Cretaceous to the time period when the marine sediments were deposited. The detailed sediment stratigraphy at our survey locations is unknown due to their inaccessibility and our MT data are unable to resolve thin evaporite deposits, but the geochemistry measured at SLW does not indicate an evaporite source (*25*). Cryoconcentration, the freezing of seawater that preferentially freezes fresher water onto the ice sheet base and leaves saltier water behind, could also explain our observations. Cryoconcentration is typically thought to occur at the continent-ocean boundary of continental ice sheets and glaciers (*67*) but could potentially occur when an ice shelf transitions from floating to grounded, as is the case for WIS. Cryoconcentration could contribute to the enhanced salinity that we observe within the sediments below WIS, but disentangling the potential causes of enhanced salinity will require hydrologic modeling.

Water-column depth calculation

The water column depth is equivalent to the vertically integrated porosity of a given sediment thickness. This assumes that the pore spaces are saturated with water. We computed the integrated porosity for the range of sediment thickness estimates from both MT and seismic

(0.5–1.9 km) using the same porosity model for our Archie's calculation to obtain water column depth estimates of 220–820 m.

Rationale for submarine groundwater discharge at WGZ

Below the floating ice at WGZ, the salinity of the groundwater in the top 200 m of sediments is 14–86% lower than seawater (Fig. 2D), which requires ongoing lateral flow of groundwater across the grounding line; otherwise saltier, denser seawater would replace it (*29*). This indicates that submarine groundwater discharge (SGD), groundwater flow from the seafloor into the ocean, is occurring beneath WGZ.

Seismic P-wave Receiver Function Analysis

We used broadband seismic data from 53 stations acquired during short-term deployments (~ 1–2 months) during the 2010/2011 and 2011/2012 Antarctic field seasons. These relatively dense deployments were designed to study the stick-slip behavior of WIS, including microseismicity (*68*) and abrupt ice stream motion recorded by each instrument's horizontal channels (*69*, *70*).

Broadband seismic deployments for the study of Earth structure typically span several years to facilitate sufficient data required for many seismic analysis techniques. However, short-term deployments such as those on WIS can be used for a subset of seismic imaging techniques, such as receiver function analysis (*70*, *71*). The receiver function technique is a standard method for investigating subsurface structure using Ps conversion produced by sharp discontinuities in the subsurface. Ps conversions are isolated by deconvolving the vertical component from the radial component recordings of teleseismic earthquakes (*72*). For the WIS datasets, we analyzed all

earthquakes > M_w 5.8 and in the epicentral range between 30 and 90 degrees. We computed receiver functions using the iterative deconvolution method (*73*). All receiver functions were then visually examined for data quality and stacked. The number of suitable events at each station varied from 2 to 5.

Receiver functions are most commonly used to map crustal structure using the strong Ps conversions associated with the Moho discontinuity. Figure S2A shows a synthetic receiver function computed for 22 km thick crust highlighting clear Ps conversion and Moho multiples. However, receiver functions deployed on ice sheets are often dominated by ice-sheet reverberations that partially mask Moho arrivals (*74*). Figure S2B shows a synthetic receiver function for a 22 km crust with 750 m thick ice layer (typical of WIS), the major crustal seismic phases are obscured by the ice sheet reverberations. Additionally, if present, subglacial sediments can produce additional reverberations that may contribute significantly to the receiver function (Fig. S2C). When the ice thickness beneath a station is well known (as for the stations studied here), the presence of a thick (>100 m) package of low velocity sediments is easily recognizable due to the poor representation of the observed waveform by an ice over crust model. Figure S2D shows an example receiver function from the center of the network at station BB01 where the ice thickness is approximately 750 m. Casual inspection reveals that the observed receiver function is not well modeled without a sediment layer underlying the ice sheet.

We used these reverberations to estimate sediment thickness at all stations (Table S4) by comparing the observed receiver functions with synthetic receiver functions. Similar to previous work, this is done by computing synthetic waveforms across a range of sediment thicknesses and

V_p/V_s ratios. We estimate the quality of fit by measuring the correlation coefficient between the observed and synthetic receiver functions. Previous work (*71, 75*) used relatively high-frequency receiver functions (~ 1 Hz) to estimate sediment layer thickness by modeling the first few seconds of the signal. Since the early part of the signal is not influenced by deeper crustal arrivals, such as those from the Moho, the sediment layer can be modeled using a crust half-space as the lower boundary condition. However, the relatively high impedance contrast across the ice-sediment interface on WIS (*64*) results in large amplitude ice reverberations that obscure the reverberations arising from the sediment-bedrock interface at high frequencies. Thus, we apply a low-pass filter at 0.25 Hz and model a longer duration of signal (25 seconds). This method requires performing the grid search across a range of both sediment and crustal thickness. Figure S3A shows the best-fit for station BB01 located within the center of the array. The optimal fit is achieved with a crustal thickness of 22 km with the quality of the fit degrading for lower and higher crustal thickness values (Fig. S3B). This optimal fit is achieved with a sediment thickness of 750 m and a V_p/V_s ratio of 2.4 (Fig. S3C). As is common in receiver function studies, a trade-off exists between the V_p/V_s ratio and depth to interface, allowing for a range of ~ ± 200 m sediment thicknesses to adequately describe the data. Although distorted and delayed by ice and sediment reverberations, station BB01 has a well-defined Moho multiple that arrives between 11 s and 16 s after the direct P-wave (Fig. S2D). In contrast, some sites have more well-developed reverberations that completely obscure distinct arrivals from the Moho (Fig. S3D). In such cases, a trade-off between crust and sediment thickness prevents a clear estimate of crustal thickness (Fig. S3E). To resolve this ambiguity and since we observe no regional trends in crustal thickness, we estimate sediment thickness at all sites using a crustal thickness of 22 km, the median value for all 53 locations (Fig. 1A).
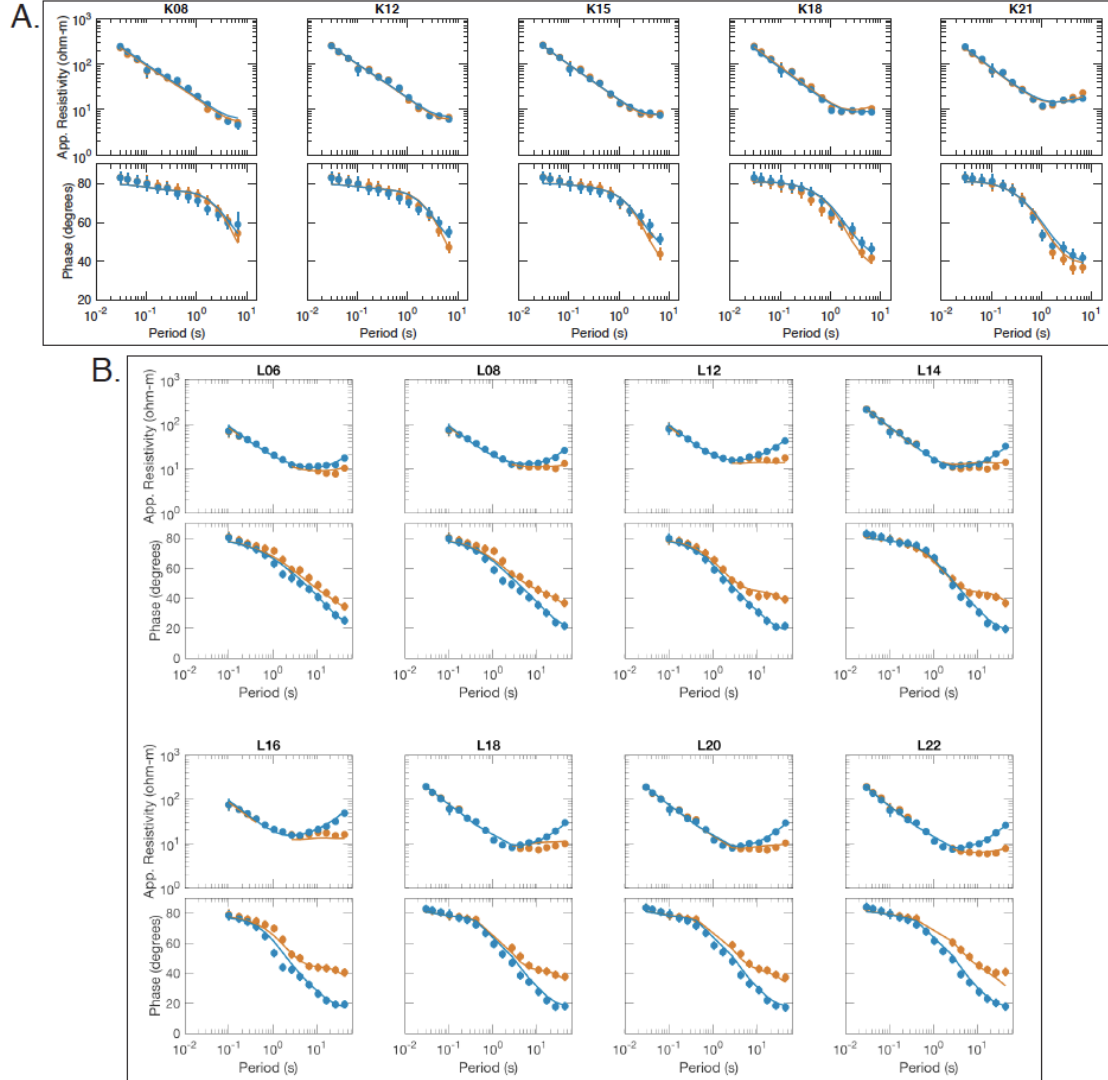
Fig. S1. MT response functions.

Apparent resistivity and phase data (circles) with model responses (lines) for the (**A**) SLW

profile (**B**) WGZ profile of MT stations inverted to obtain resistivity models in Figs. 2A, 2B.

Alphanumeric station names are listed above each plot, where station names starting with K

correspond to SLW stations and station names starting with L correspond to WGZ stations.

Stations are ordered from furthest upstream to furthest downstream (i.e., K08 and L06 are the

furthest upstream stations and K21 and L22 are the furthest downstream stations). Z_{xy}

polarization data (TE mode) are shown in red and Z_{yx} polarization data (TM mode) are shown in
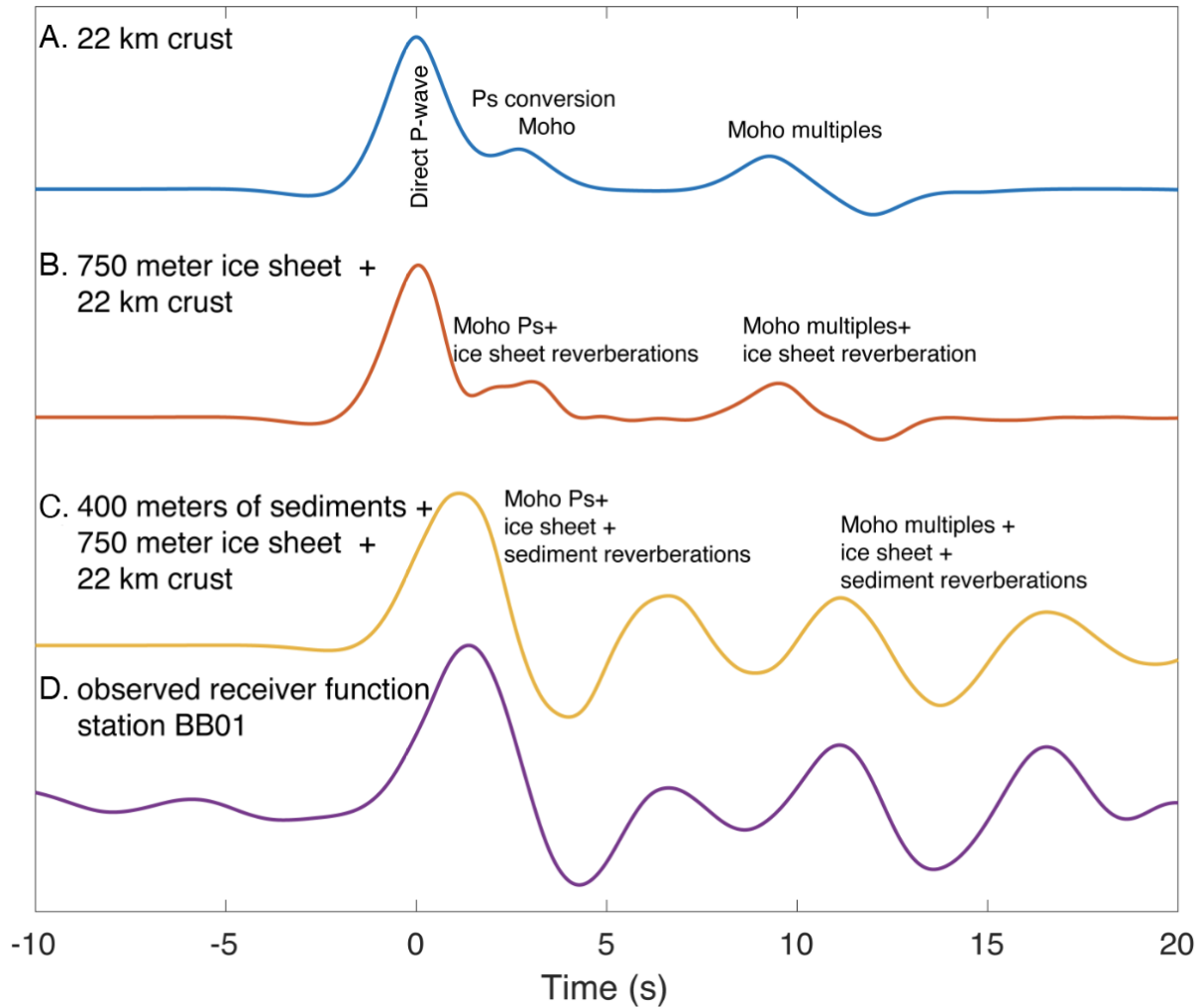
blue.

Fig. S2. Influence of ice sheet and sediments on receiver functions.

(**A**) Synthetic receiver function for a two-layer model of a 22 km crust over a mantle half-space.

(**B**) Synthetic receiver function with the addition of a 750 m thick ice column over the crust. (**C**)

Synthetic receiver function with the addition of 400 m of subglacial sediments under the ice

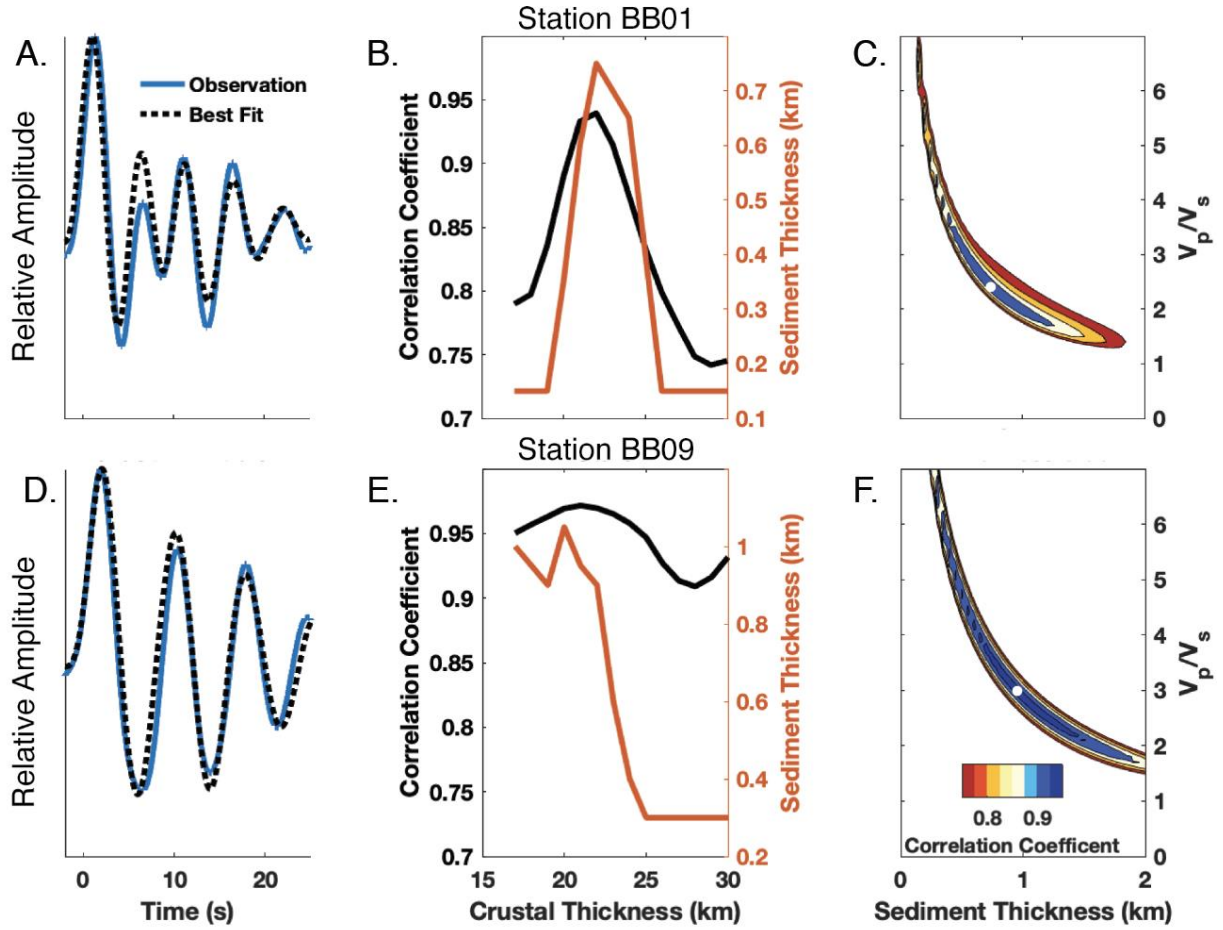stream. (**D**) Observed receiver function at station BB01.

Fig. S3. Grid search to estimate sediment thickness beneath stations BB01 and BB09.

(**A,D**) Observed and best-fit synthetic receiver functions. (**B,E**) Peak correlation and sediment thickness versus crustal thickness. (**C,F**) Peak correlation coefficient as a function of sediment thickness and V_p/V_s ratio for optimal crustal thickness. White circle shows the best fit of parameters used to compute synthetic receiver function in panels (A) and (D).
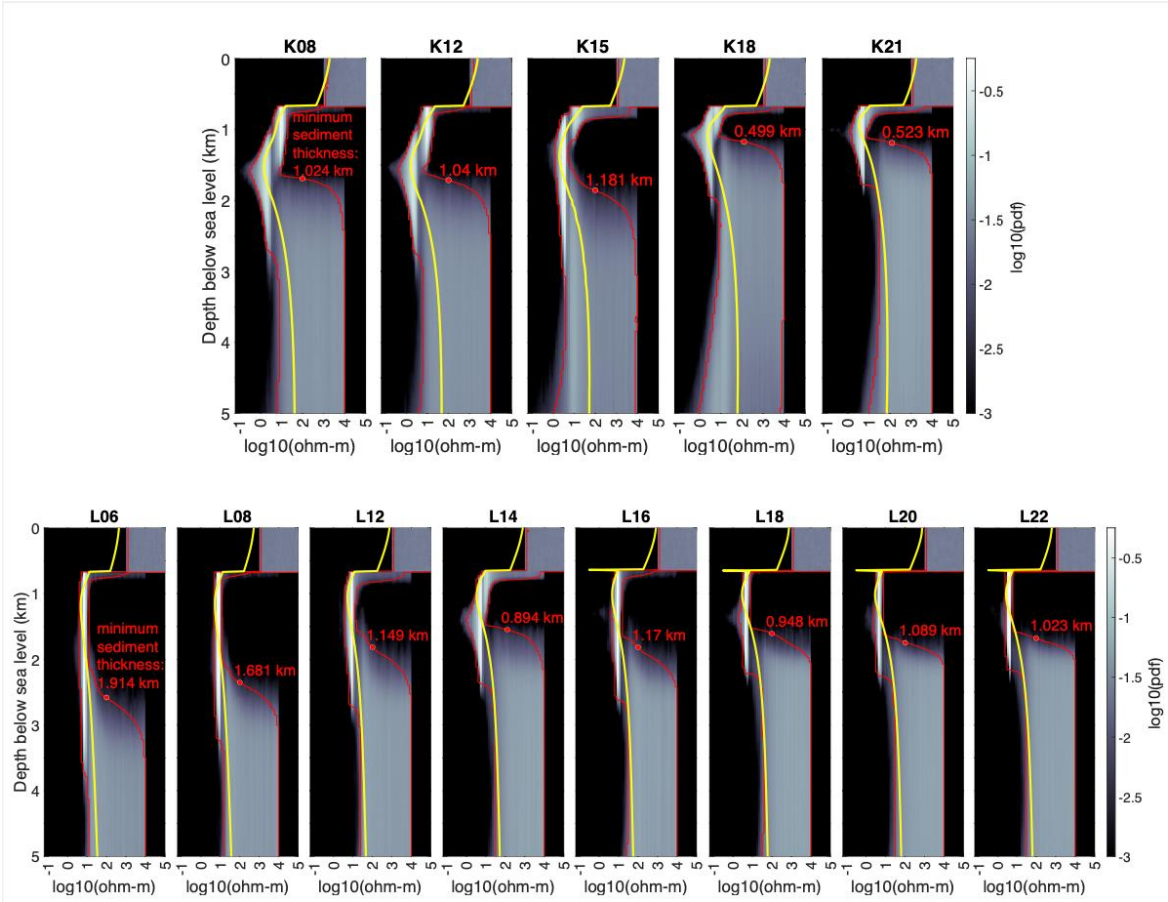
Fig. S4. Bayesian 1D inversions and sediment thickness estimates.

Bayesian 1D inversions of Z_{yx} data for each K profile station at SLW (top row) and each L profile station at WGZ (bottom row). Shaded colors show the resistivity probability density functions (PDF) as a function of depth. Red lines indicate the 5th (left) and 95th (right) percentiles of the probability density and thus the space between is the 90% credible interval. For each station, a 1D profile extracted from the 2D inversions at the station location (Figs. 2A, 2B) is shown as a yellow line. These results show that the MT data require low electrical resistivity below the ice bed, and a resistivity increase at depth. The minimum sediment thickness determined by the depth at which the 95th percentile is greater than or equal to 100 ohm-m is indicated by a red dot and red text.
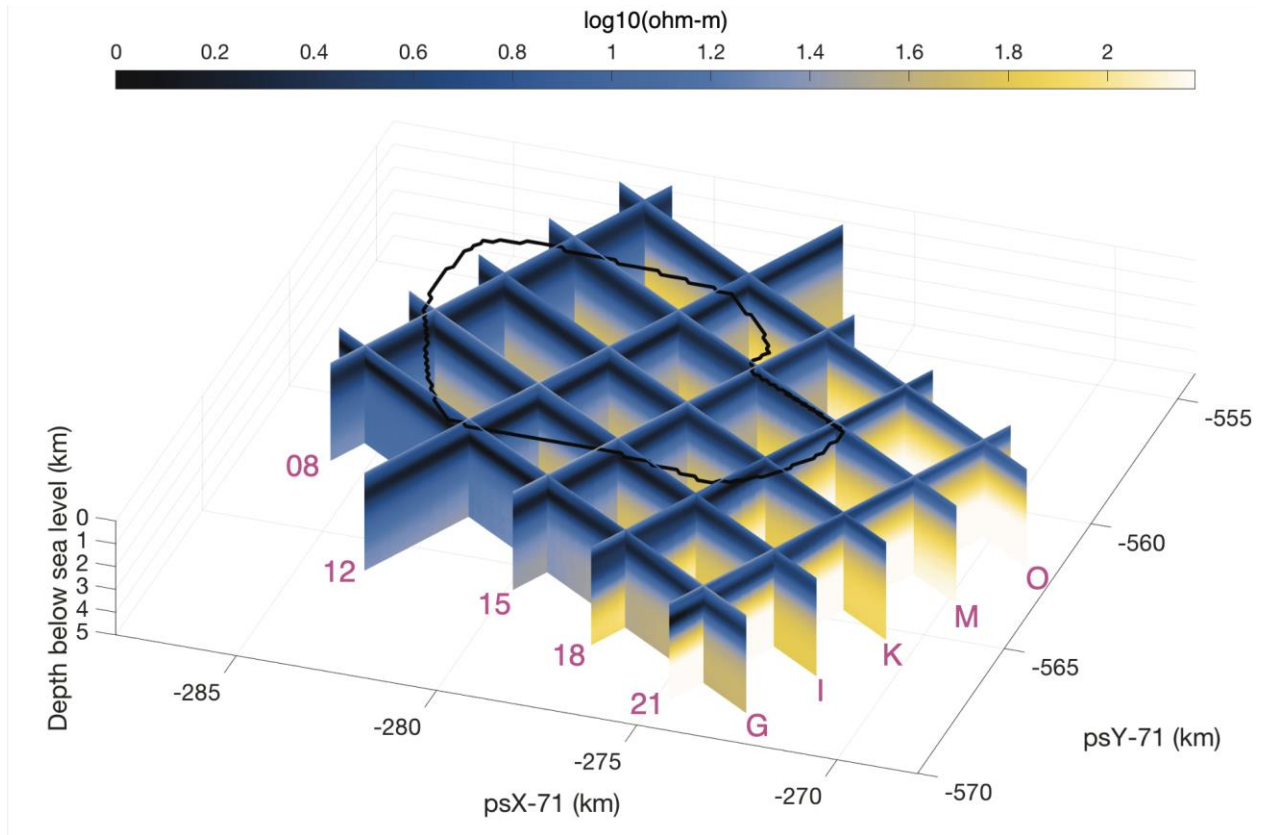
Fig. S5. SLW MT inversion results.

Fence plot of all 2D resistivity models obtained using a gradient-based smoothing method plotted as a function of position and depth for SLW. The color map shows the resistivity and is the same as that used in Figure 2A. Each resistivity model is plotted to a depth of 5 km below sea level, and we have removed the ice layer from each 2D model to allow for better viewing of the sub-ice structure. Survey lines are assigned a letter or a number, noted in pink. Letters correspond to survey lines that are approximately parallel to ice flow and numbers correspond to the lines that are approximately perpendicular to ice flow. The SLW lake outline (*20*) is shown at 0.8 km depth in black. Projection is south polar stereographic with a standard latitude of 71° S (EPSG 3031).
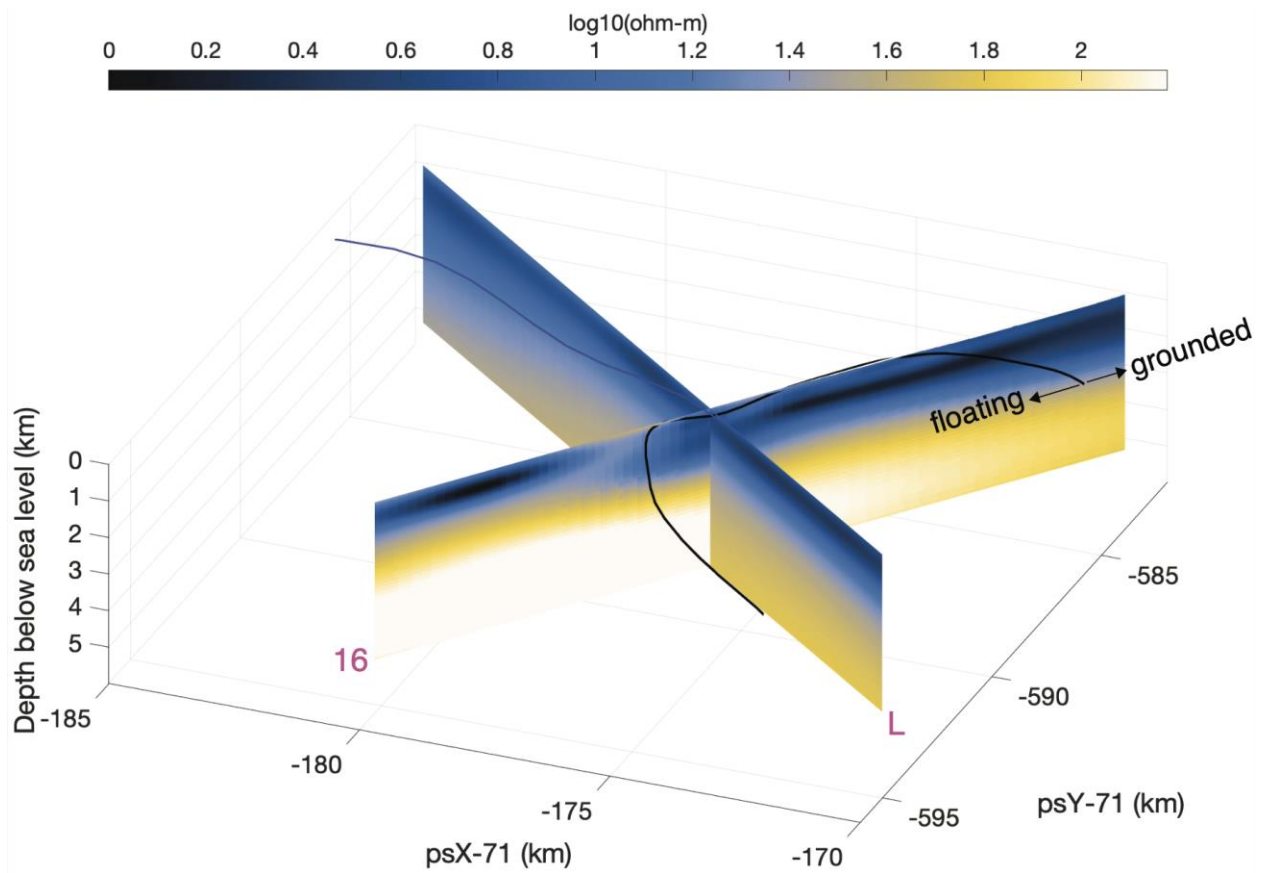
Fig. S6. WGZ MT inversion results.

Fence plot of both 2D resistivity models obtained using a gradient based smoothing method plotted as a function of position and depth for WGZ. The color map shows the resistivity and is the same as that used in Figure 2B. Each resistivity model is plotted to a depth of 5 km below sea level, and we have removed the ice layer from each 2D model to allow for better viewing of the sub-ice structure. Like SLW, survey lines are assigned a letter or a number, noted in pink. Letters correspond to survey lines that are approximately parallel to ice flow and numbers correspond to the lines that are approximately perpendicular to ice flow. Grounding line (*46*) is shown at 0.75 km depth shown in black. Blue line is the estimates water flow path for the shallow system (*42*). Projection is south polar stereographic with a standard latitude of 71° S (EPSG 3031).
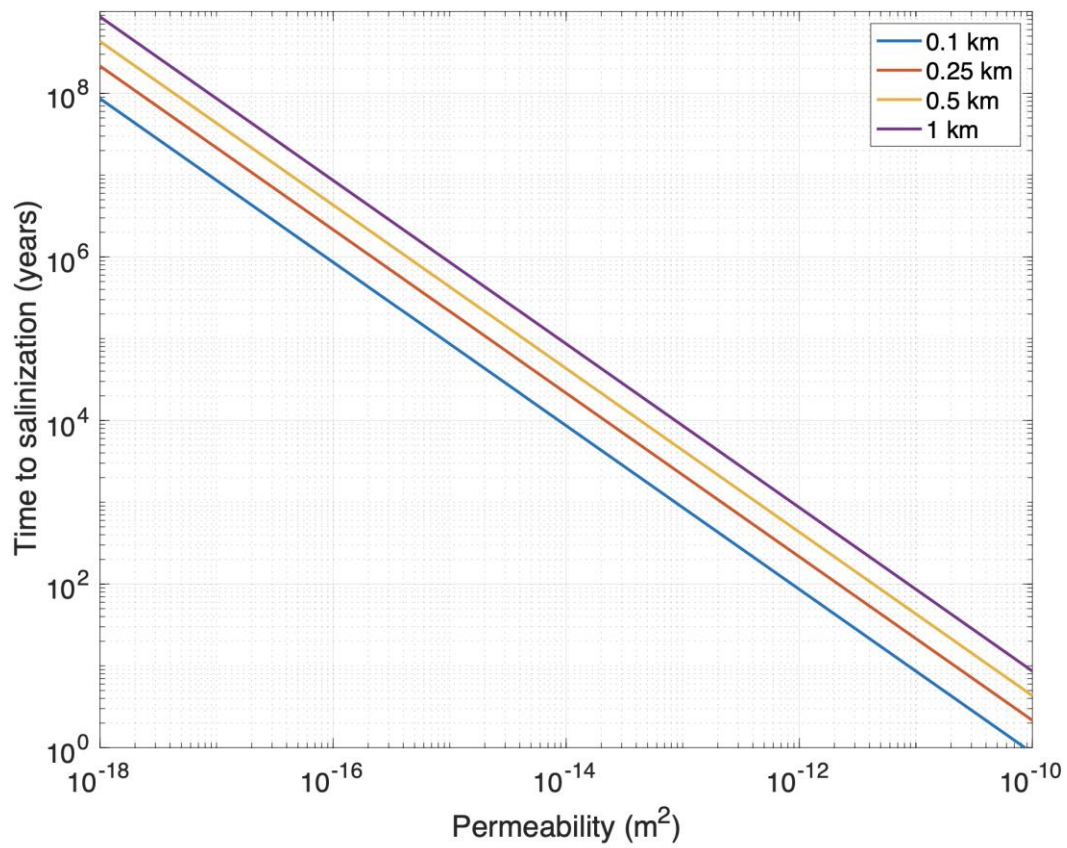
Fig. S7. Time to salinization for given sediment thickness and permeability.

We use equations 14 and 15 from ref. (*35*) to compute times for different sediment thickness

values, shown as colored lines.

Table S1. MT data wind pre-filtering scheme.

Pre-filtering scheme showing wind speed ranges used to determine the noisy period bands to
omit from the MT spectral coefficient data prior to the statistical impedance estimation process.

Wind speed (knots)	Periods (s) removed
0–5	none
5–10	0.25–20
10–15	0.013–50
15+	all

Table S2. Number of MT data and free parameters for each SLW 2D inversion line.

Line	Number of data	Number of free parameters
08	225	30545
12	360	34025
15	260	30610
18	212	30564
21	224	30611
G	248	34204
I	236	34119
K	260	34007
M	216	43044
O	231	33940

Table S3. Number of MT data and free parameters for each WGZ 2D inversion line.

Line	Number of Data	Number of free parameters
16	216 (TM only)	35268
L	248 (TM only)	36879

Table S4. Passive seismic sediment thickness estimates.

Passive seismic station names, locations, and sediment thickness estimates plotted in Fig. 1A. Locations are listed using both south polar stereographic (PS71 X, PS71 Y) projection with a standard latitude of 71° S (EPSG 3031) and geographic coordinates (latitude, longitude).

Station	PS71 X (m)	PS71 Y (m)	Latitude (°)	Longitude (°)	Sediment Thickness (km)
BB01	-230730	-575791	-84.295500	-158.163120	0.75
BB02	-220631	-569727	-84.381297	-158.830740	1.15
BB03	-239400	-582357	-84.209702	-157.653020	0.65
BB04	-248107	-592223	-84.095403	-157.269150	1.35
BB05	-211990	-577884	-84.339202	-159.855030	0.9
BB06	-249800	-558019	-84.377403	-155.884090	0.95
BB07	-239825	-568766	-84.323403	-157.136870	0.65
BB08	-199824	-569096	-84.452899	-160.652540	1.4
BB09	-215560	-566587	-84.424903	-159.170510	0.9
BB10	-230710	-602120	-84.070504	-159.035020	1.3
BB11	-229621	-565611	-84.385998	-157.904330	0.85
BB12	-206551	-592391	-84.230603	-160.777690	1
BB13	-212303	-562849	-84.467598	-159.333850	1.4
BB14	-256415	-577393	-84.190201	-156.054430	1.3
BB15	-222642	-582979	-84.261098	-159.097940	1
BB16	-215488	-551209	-84.556902	-158.647630	1.1

BB17	-233281	-544475	-84.552197	-156.807230	1.75
IP01	-200764	-580485	-84.351302	-160.921770	1.75
IP03	-224361	-575100	-84.322904	-158.687990	1.15
IP04	-230234	-568970	-84.355299	-157.969260	0.9
IP06	-231767	-591208	-84.160403	-158.593690	1.1
IP08	-228291	-574126	-84.318001	-158.315640	0.8
IP09	-229072	-574566	-84.311595	-158.263470	0.65
IP10	-236366	-556016	-84.443598	-156.969340	1.15
IP11	-231241	-581638	-84.243901	-158.318790	0.65
IP12	-214606	-584987	-84.269700	-159.854130	1.25
IP13	-225934	-571558	-84.347897	-158.431360	1.3
IP14	-211326	-570585	-84.404196	-159.677020	0.5
IP16	-224996	-571284	-84.353399	-158.503360	1.1
IP17	-229040	-573781	-84.318399	-158.239270	0.7
IP18	-219282	-560038	-84.468700	-158.617250	1.2
IP19	-214888	-600952	-84.131004	-160.324000	1.25
IP21	-227308	-640429	-83.751401	-160.458660	1.2
S001	-261220	-537962	-84.500000	-154.100010	0.85
S003	-224689	-542447	-84.599998	-157.500000	1.15
S008	-227752	-555317	-84.480003	-157.700000	0.8
S009	-241845	-545755	-84.510002	-156.100010	1.45
S010	-229713	-572150	-84.330002	-158.125000	1.5
S011	-257031	-564002	-84.300003	-155.500000	1.1

S002	-254279	-552546	-84.406166	-155.288340	0.9
GS04	-236556	-556611	-84.437887	-156.974830	1.05
GS05	-208324	-543132	-84.649836	-159.015160	1.5
GS07	-220209	-570547	-84.375671	-158.895350	1.1
S008	-212036	-562815	-84.468755	-159.356510	1.6
GS09	-202837	-556298	-84.554234	-159.967170	1.3
S010	-194931	-549873	-84.634329	-160.480490	1.3
GS11	-230998	-602496	-84.066334	-159.023090	1.2
GS13	-180244	-564027	-84.554203	-162.277870	1
GS14	-227619	-617105	-83.951732	-159.753520	0.9
GS15	-190325	-593354	-84.269501	-162.215770	0.85
GS16	-234582	-629668	-83.821397	-159.567190	1.1
GS17	-215815	-628780	-83.887107	-161.056340	0.95
rGS18	-222954	-640127	-83.767270	-160.796950	0.65

References and Notes

1. M. R. Bennett, Ice streams as the arteries of an ice sheet: Their mechanics, stability and significance. *Earth Sci. Rev.* **61**, 309–339 (2003). doi:10.1016/S0012-8252(02)00130-7

2. M. Bougamont, S. Price, P. Christoffersen, A. J. Payne, Dynamic patterns of ice stream flow in a 3-D higher-order ice sheet model with plastic bed and simplified hydrology. *J. Geophys. Res.* **116**, F04018 (2011). doi:10.1029/2011JF002025

3. D. D. Blankenship, C. R. Bentley, S. T. Rooney, R. B. Alley, Seismic measurements reveal a saturated porous layer beneath an active Antarctic ice stream. *Nature* **322**, 54–57 (1986). doi:10.1038/322054a0

4. K. Christianson, R. W. Jacobel, H. J. Horgan, S. Anandakrishnan, R. B. Alley, Subglacial Lake Whillans — Ice-penetrating radar and GPS observations of a shallow active reservoir beneath a West Antarctic ice stream. *Earth Planet. Sci. Lett.* **331–332**, 237–245 (2012). doi:10.1016/j.epsl.2012.03.013

5. B. Kamb, "Basal zone of the West Antarctic Ice Streams and its role in lubrication of their rapid motion" in *The West Antarctic Ice Sheet Behavior and Environment*, R. B. Alley, R. A. Bindschadle, Eds. (Antarctic Research Series, vol. 77, American Geophysical Union, 2001), pp. 157–199.

6. M. J. Siegert, B. Kulessa, M. Bougamont, P. Christoffersen, K. Key, K. R. Andersen, A. D. Booth, A. M. Smith, Antarctic subglacial groundwater: A concept paper on its measurement and potential influence on ice flow. *Spec. Publ. Geol. Soc. London* **461**, 197–213 (2018). doi:10.1144/SP461.8

7. R. E. Bell, D. D. Blankenship, C. A. Finn, D. L. Morse, T. A. Scambos, J. M. Brozena, S. M. Hodge, Influence of subglacial geology on the onset of a West Antarctic ice stream from aerogeophysical observations. *Nature* **394**, 58–62 (1998). doi:10.1038/27883

8. S. Anandakrishnan, D. D. Blankenship, R. B. Alley, P. L. Stoffa, Influence of subglacial geology on the position of a West Antarctic ice stream from seismic observations. *Nature* **394**, 62–65 (1998). doi:10.1038/27889

9. M. Studinger, R. E. Bell, D. D. Blankenship, C. A. Finn, R. A. Arko, D. L. Morse, I. Joughin, Subglacial sediments: A regional geological template for ice flow in West Antarctica. *Geophys. Res. Lett.* **28**, 3493–3496 (2001). doi:10.1029/2000GL011788

10. C. Gustafson, H. Fricker, K. Key, M. Siegfried, Wideband magnetotelluric responses from Whillans Ice Stream, West Antarctica. U.S. Antarctic Program (USAP) Data Center (2022); https://doi.org/10.15784/601526.

11. P. Winberry, S. Anandakrishnan, D. Wiens, Geophysical study of ice stream stick-slip dynamics. International Federation of Digital Seismograph Networks (2010); https://doi.org/10.7914/SN/2C_2010.

12. S. Tulaczyk, I. Joughin, S. Schwartz, J. Walter, Elevation change anomalies in West Antarctica and dynamics of subglacial water beneath ice streams and their tributaries. International Federation of Digital Seismograph Networks (2010); https://doi.org/10.7914/SN/1D_2010.

13. T. M. Kyrke-Smith, A. C. Fowler, Subglacial swamps. *Proc. Math. Phys. Eng. Sci.* **470**, 20140340 (2014). [Medline](#)

14. R. Kirsch, Ed., *Groundwater Geophysics: A Tool for Hydrogeology* (Springer, 2006).

15. K. Key, M. R. Siegfried, The feasibility of imaging subglacial hydrology beneath ice streams with ground-based electromagnetics. *J. Glaciol.* **63**, 755–771 (2017). [doi:10.1017/jog.2017.36](#)

16. N. Foley, S. M. Tulaczyk, D. Grombacher, P. T. Doran, J. Mikucki, K. F. Myers, N. Foged, H. Dugan, E. Auken, R. Virginia, Evidence for pathways of concentrated submarine groundwater discharge in East Antarctica from helicopter-borne electrical resistivity measurements. *Hydrology* **6**, 54 (2019). [doi:10.3390/hydrology6020054](#)

17. A. D. Chave, A. G. Jones, Eds., *The Magnetotelluric Method Theory and Practice* (Cambridge Univ. Press, 2012).

18. G. J. Hill, On the use of electromagnetics for Earth imaging of the polar regions. *Surv. Geophys.* **41**, 5–45 (2019). [doi:10.1007/s10712-019-09570-8](#)

19. P. Christoffersen, M. Bougamont, S. P. Carter, H. A. Fricker, S. Tulaczyk, Significant groundwater contribution to Antarctic ice streams hydrologic budget. *Geophys. Res. Lett.* **41**, 2003–2010 (2014). [doi:10.1002/2014GL059250](#)

20. H. A. Fricker, T. Scambos, Connected subglacial lake activity on lower Mercer and Whillans Ice Streams, West Antarctica, 2003–2008. *J. Glaciol.* **55**, 303–315 (2009). [doi:10.3189/002214309788608813](#)

21. H. J. Horgan, R. B. Alley, K. Christianson, R. W. Jacobel, S. Anandakrishnan, A. Muto, L. H. Beem, M. R. Siegfried, Estuaries beneath ice sheets. *Geology* **41**, 1159–1162 (2013). [doi:10.1130/G34654.1](#)

22. H. J. Horgan, S. Anandakrishnan, R. W. Jacobel, K. Christianson, R. B. Alley, D. S. Heeszel, S. Picotti, J. I. Walter, Subglacial Lake Whillans — Seismic observations of a shallow active reservoir beneath a West Antarctic ice stream. *Earth Planet. Sci. Lett.* **331–332**, 201–209 (2012). [doi:10.1016/j.epsl.2012.02.023](#)

23. B. C. Christner, J. C. Priscu, A. M. Achberger, C. Barbante, S. P. Carter, K. Christianson, A. B. Michaud, J. A. Mikucki, A. C. Mitchell, M. L. Skidmore, T. J. Vick-Majors, WISSARD Science Team, A microbial ecosystem beneath the West Antarctic ice sheet. *Nature* **512**, 310–313 (2014). [doi:10.1038/nature13667](#) [Medline](#)

24. C. B. Begeman, S. M. Tulaczyk, O. J. Marsh, J. A. Mikucki, T. P. Stanton, T. O. Hodson, M. R. Siegfried, R. D. Powell, K. Christianson, M. A. King, Ocean stratification and low melt rates at the Ross Ice Shelf grounding zone. *J. Geophys. Res. Oceans* **123**, 7438–7452 (2018). [doi:10.1029/2018JC013987](#)

25. A. B. Michaud, M. L. Skidmore, A. C. Mitchell, T. J. Vick-Majors, C. Barbante, C. Turetta, W. vanGelder, J. C. Priscu, Solute sources and geochemical processes in Subglacial Lake Whillans, West Antarctica. *Geology* **44**, 347–350 (2016). [doi:10.1130/G37639.1](#)

26. H. J. Horgan, K. Christianson, R. W. Jacobel, S. Anandakrishnan, R. B. Alley, Sediment deposition at the modern grounding zone of Whillans Ice Stream, West Antarctica. *Geophys. Res. Lett.* **40**, 3934–3939 (2013). [doi:10.1002/grl.50712](#)

27. Materials and methods are available as supplementary materials.

28. A. Muto, K. Christianson, H. J. Horgan, S. Anandakrishnan, R. B. Alley, Bathymetry and geological structures beneath the Ross Ice Shelf at the mouth of Whillans Ice Stream, West Antarctica, modeled from ground-based gravity measurements. *J. Geophys. Res. Solid Earth* **118**, 4535–4546 (2013). doi:10.1002/jgrb.50315

29. R. M. McKay *et al*., "Expedition 374 preliminary report: Ross Sea West Antarctica Ice Sheet history" (International Ocean Discovery Program, 2018).

30. C. B. Begeman, S. M. Tulaczyk, A. T. Fisher, Spatially variable geothermal heat flux in West Antarctica: Evidence and implications. *Geophys. Res. Lett.* **44**, 9823–9832 (2017). [doi:10.1002/2017GL075579](doi:10.1002/2017GL075579)

31. S. Tulaczyk, J. A. Mikucki, M. R. Siegfried, J. C. Priscu, C. G. Barcheck, L. H. Beem, A. Behar, J. Burnett, B. C. Christner, A. T. Fisher, H. A. Fricker, K. D. Mankoff, R. D. Powell, F. Rack, D. Sampson, R. P. Scherer, S. Y. Schwartz, WISSARD at Subglacial Lake Whillans, West Antarctica: Scientific operations and initial observations. *Ann. Glaciol.* **55**, 51–58 (2014). [doi:10.3189/2014AoG65A009](doi:10.3189/2014AoG65A009)

32. J. C. Priscu, J. Kalin, J. Winans, T. Campbell, M. R. Siegfried, M. Skidmore, J. E. Dore, A. Leventer, D. M. Harwood, D. Duling, R. Zook, J. Burnett, D. Gibson, E. Krula, A. Mironov, J. McManis, G. Roberts, B. E. Rosenheim, B. C. Christner, K. Kasic, H. A. Fricker, W. B. Lyons, J. Barker, M. Bowling, B. Collins, C. Davis, A. Gagnon, C. Gardner, C. Gustafson, O.-S. Kim, W. Li, A. Michaud, M. O. Patterson, M. Tranter, R. Venturelli, T. Vick-Majors, C. Elsworth, Scientific access into Mercer Subglacial Lake: Scientific objectives, drilling operations and initial observations. *Ann. Glaciol.* **62**, 340–352 (2021). [doi:10.1017/aog.2021.10](doi:10.1017/aog.2021.10)

33. R. A. Venturelli, M. R. Siegfried, K. A. Roush, W. Li, J. Burnett, R. Zook, H. A. Fricker, J. C. Priscu, A. Leventer, B. E. Rosenheim, Mid-Holocene grounding line retreat and readvance at Whillans Ice Stream, West Antarctica. *Geophys. Res. Lett.* **47**, e2020GL088476 (2020). [doi:10.1029/2020GL088476](doi:10.1029/2020GL088476)

34. J. Kingslake, R. P. Scherer, T. Albrecht, J. Coenen, R. D. Powell, R. Reese, N. D. Stansell, S. Tulaczyk, M. G. Wearing, P. L. Whitehouse, Extensive retreat and re-advance of the West Antarctic Ice Sheet during the Holocene. *Nature* **558**, 430–434 (2018). [doi:10.1038/s41586-018-0208-x](doi:10.1038/s41586-018-0208-x) Medline

35. V. E. A. Post, H. Kooi, Rates of salinization by free convection in high-permeability sediments: Insights from numerical modeling and application to the Dutch coastal area. *Hydrogeol. J.* **11**, 549–559 (2003). [doi:10.1007/s10040-003-0271-7](doi:10.1007/s10040-003-0271-7)

36. R. P. Scherer, Quaternary and Tertiary microfossils from beneath Ice Stream B: Evidence for a dynamic West Antarctic Ice Sheet history. *Global Planet. Change* **4**, 395–412 (1991). [doi:10.1016/0921-8181(91)90005-H](doi:10.1016/0921-8181(91)90005-H)

37. J. M. Lemieux, E. A. Sudicky, W. R. Peltier, L. Tarasov, Dynamics of groundwater recharge and seepage over the Canadian landscape during the Wisconsinian glaciation. *J. Geophys. Res.* **113**, F01011 (2008). [doi:10.1029/2007JF000838](doi:10.1029/2007JF000838)

38. B. T. Gooch, D. A. Young, D. D. Blankenship, Potential groundwater and heterogeneous heat source contributions to ice sheet dynamics in critical submarine basins of East

Antarctica. *Geochem. Geophys. Geosyst.* **17**, 395–409 (2016). doi:10.1002/2015GC006117

39. A. B. Michaud, J. E. Dore, A. M. Achberger, B. C. Christner, A. C. Mitchell, M. L. Skidmore, T. J. Vick-Majors, J. C. Priscu, Microbial oxidation as a methane sink beneath the West Antarctic Ice Sheet. *Nat. Geosci.* **10**, 582–586 (2017). doi:10.1038/ngeo2992

40. I. P. G. Marshall, S. M. Karst, P. H. Nielsen, B. B. Jørgensen, Metagenomes from deep Baltic Sea sediments reveal how past and present environmental conditions determine microbial community composition. *Mar. Genomics* **37**, 58–68 (2018). doi:10.1016/j.margen.2017.08.004 Medline

41. T. J. Vick-Majors, A. B. Michaud, M. L. Skidmore, C. Turetta, C. Barbante, B. C. Christner, J. E. Dore, K. Christianson, A. C. Mitchell, A. M. Achberger, J. A. Mikucki, J. C. Priscu, Biogeochemical connectivity between freshwater ecosystems beneath the West Antarctic Ice Sheet and the sub-ice marine environment. *Global Biogeochem. Cycles* **34**, 1–17 (2020). doi:10.1029/2019GB006446

42. S. P. Carter, H. A. Fricker, The supply of subglacial meltwater to the grounding line of the Siple Coast, West Antarctica. *Ann. Glaciol.* **53**, 267–280 (2012). doi:10.3189/2012AoG60A119

43. T. Uemura, M. Taniguchi, K. Shibuya, Submarine groundwater discharge in Lützow-Holm Bay, Antarctica. *Geophys. Res. Lett.* **38**, L08402 (2011). doi:10.1029/2010GL046394

44. J. Mouginot, E. Rignot, B. Scheuchl, Continent-wide, interferometric SAR phase, mapping of Antarctic ice velocity. *Geophys. Res. Lett.* **46**, 9710–9718 (2019). doi:10.1029/2019GL083826

45. T. A. Scambos, T. M. Haran, M. A. Fahnestock, T. H. Painter, J. Bohlander, MODIS-based Mosaic of Antarctica (MOA) data sets: Continent-wide surface morphology and snow grain size. *Remote Sens. Environ.* **111**, 242–257 (2007). doi:10.1016/j.rse.2006.12.020

46. M. A. Depoorter, J. L. Bamber, J. A. Griggs, J. T. M. Lenaerts, S. R. M. Ligtenberg, M. R. van den Broeke, G. Moholdt, Calving fluxes and basal melt rates of Antarctic ice shelves. *Nature* **502**, 89–92 (2013). doi:10.1038/nature12567 Medline

47. P. E. Wannamaker, J. A. Stodt, S. L. Olsen, Dormant state of rifting below the Byrd Subglacial Basin, West Antarctica, implied by magnetotelluric (MT) profiling. *Geophys. Res. Lett.* **23**, 2983–2986 (1996). doi:10.1029/96GL02887

48. P. E. Wannamaker, J. A. Stodt, L. Pellerin, S. L. Olsen, D. B. Hall, Structure and thermal regime beneath the South Pole region, East Antarctica, from magnetotelluric measurements. *Geophys. J. Int.* **157**, 36–54 (2004). doi:10.1111/j.1365-246X.2004.02156.x

49. P. Wannamaker, G. Hill, J. Stodt, V. Maris, Y. Ogawa, K. Selway, G. Boren, E. Bertrand, D. Uhlmann, B. Ayling, A. M. Green, D. Feucht, Uplift of the central transantarctic mountains. *Nat. Commun.* **8**, 1588 (2017). doi:10.1038/s41467-017-01577-2 Medline

50. J. R. Peacock, K. Selway, Magnetotelluric investigation of the Vestfold Hills and Rauer Group, East Antarctica. *J. Geophys. Res. Solid Earth* **121**, 2258–2273 (2016). doi:10.1002/2015JB012677

51. G. D. Egbert, Robust multiple-station magnetotelluric data processing. *Geophys. J. Int.* **130**, 475–496 (1997). [doi:10.1111/j.1365-246X.1997.tb05663.x](doi:10.1111/j.1365-246X.1997.tb05663.x)

52. C. M. Swift, thesis, Massachusetts Institute of Technology (1967).

53. K. Key, MARE2DEM: A 2-D inversion code for controlled-source electromagnetic and magnetotelluric data. *Geophys. J. Int.* **207**, 571–588 (2016). [doi:10.1093/gji/ggw290](doi:10.1093/gji/ggw290)

54. M. Morlighem, E. Rignot, T. Binder, D. Blankenship, R. Drews, G. Eagles, O. Eisen, F. Ferraccioli, R. Forsberg, P. Fretwell, V. Goel, J. S. Greenbaum, H. Gudmundsson, J. Guo, V. Helm, C. Hofstede, I. Howat, A. Humbert, W. Jokat, N. B. Karlsson, W. S. Lee, K. Matsuoka, R. Millan, J. Mouginot, J. Paden, F. Pattyn, J. Roberts, S. Rosier, A. Ruppel, H. Seroussi, E. C. Smith, D. Steinhage, B. Sun, M. R. Broeke, T. D. Ommen, M. Wessem, D. A. Young, Deep glacial troughs and stabilizing ridges unveiled beneath the margins of the Antarctic ice sheet. *Nat. Geosci.* **13**, 132–137 (2020). [doi:10.1038/s41561-019-0510-8](doi:10.1038/s41561-019-0510-8)

55. B. Kulessa, a critical review of the low-frequency electrical properties of ice sheets and glaciers. *J. Environ. Eng. Geophys.* **12**, 23–36 (2007). doi:10.2113/JEEG12.1.23

56. D. Blatter, K. Key, A. Ray, C. Gustafson, R. Evans, Bayesian joint inversion of controlled source electromagnetic and magnetotelluric data to image freshwater aquifer offshore New Jersey. *Geophys. J. Int.* **218**, 1822–1837 (2019). [doi:10.1093/gji/ggz253](doi:10.1093/gji/ggz253)

57. R. Knight, A. L. Endres, in *Near-Surface Geophysics, Volume 1: Concepts and Fundamentals*, D. K. Butler, Ed. (Society of Exploration Geophysicists, 2005), pp. 31–70.

58. S. H. Ward, G. W. Hohmann, in *Electromagnetic Methods in Applied Geophysics: Volume 1, Theory*, M. N. Nabighian, Ed. (Society of Exploration Geophysicists, 1988), pp. 130–311.

59. P. N. Sen, P. A. Goode, Influence of temperature on electrical conductivity on shaly sands. *Geophysics* **57**, 89–96 (1998). [doi:10.1190/1.1443191](doi:10.1190/1.1443191)

60. E. G. Archie, Electrical resistivity log as an aid in determining some reservoir characteristics. *Trans. AIME* **146**, 54–62 (1942).

61. E. L. Lewis, R. G. Perkin, Salinity: Its definition and calculation. *J. Geophys. Res.* **83**, 466–478 (1978). [doi:10.1029/JC083iC01p00466](doi:10.1029/JC083iC01p00466)

62. M. H. Waxman, L. J. M. Smits, Electrical conductivities in oil-bearing shaly sands. *Soc. Pet. Eng. J.* **8**, 107–122 (1968). [doi:10.2118/1863-A](doi:10.2118/1863-A)

63. L. F. Athy, Density, porosity, and compaction of sedimentary rocks. *Bull. Am. Assoc. Pet. Geol.* **14**, 1–24 (1930).

64. T. Luthra, S. Anandakrishnan, J. P. Winberry, R. B. Alley, N. Holschuh, Basal characteristics of the main sticky spot on the ice plain of Whillans Ice Stream, Antarctica. *Earth Planet. Sci. Lett.* **440**, 12–19 (2016). doi:10.1016/j.epsl.2016.01.035

65. J. J. Coenen, R. P. Scherer, P. Baudoin, S. Warny, I. S. Castañeda, R. Askin, Paleogene marine and terrestrial development of the West Antarctic rift system. *Geophys. Res. Lett.* **47**, e2019GL085281 (2020). [doi:10.1029/2019GL085281](doi:10.1029/2019GL085281)

66. Y. K. Kharaka, J. S. Hanor, "Deep fluids in sedimentary basins" in *Treatise on Geochemistry*, J. I. Drever, Ed. (Elsevier, ed. 2, 2014), pp. 471–515.

67. A. Starinsky, A. Katz, The formation of natural cryogenic brines. *Geochim. Cosmochim. Acta* **67**, 1475–1484 (2003). doi:10.1016/S0016-7037(02)01295-4

68. J. P. Winberry, S. Anandakrishnan, D. A. Wiens, R. B. Alley, Nucleation and seismic tremor associated with the glacial earthquakes of Whillans Ice Stream, Antarctica. *Geophys. Res. Lett.* **40**, 312–315 (2013). doi:10.1002/grl.50130

69. M. J. Pratt, J. P. Winberry, D. A. Wiens, S. Anandakrishnan, R. B. Alley, Seismic and geodetic evidence for grounding-line control of Whillans Ice Stream stick-slip events. *J. Geophys. Res. Earth Surf.* **119**, 333–348 (2014). doi:10.1002/2013JF002842

70. J. I. Walter, E. E. Brodsky, S. M. Tulaczyk, S. Y. Schwartz, R. Pettersson, Transient slip events from near-field seismic and geodetic data on a glacier fault, Whillans Ice Plain, West Antarctica. *J. Geophys. Res. Earth Surf.* **116**, 1–13 (2011).

71. S. Anandakrishnan, J. P. Winberry, Antarctic subglacial sedimentary layer thickness from receiver function analysis. *Global Planet. Change* **42**, 167–176 (2004). doi:10.1016/j.gloplacha.2003.10.005

72. C. A. Langston, Structure under Mount Rainier, Washington, inferred from teleseismic body waves. *J. Geophys. Res.* **84**, 4749–4762 (1979). doi:10.1029/JB084iB09p04749

73. J. P. Ligorría, C. J. Ammon, Iterative deconvolution and receiver-function estimation. *Bull. Seismol. Soc. Am.* **89**, 1395–1400 (1999). doi:10.1785/BSSA0890051395

74. J. P. Winberry, S. Anandakrishnan, Crustal structure of the West Antarctic rift system and Marie Byrd Land hotspot. *Geology* **32**, 977–980 (2004). doi:10.1130/G20768.1

75. J. Chaput, R. C. Aster, A. Huerta, X. Sun, A. Lloyd, D. Wiens, A. Nyblade, S. Anandakrishnan, J. P. Winberry, T. Wilson, The crustal thickness of West Antarctica. *J. Geophys. Res. Solid Earth* **119**, 378–395 (2014). doi:10.1002/2013JB010642